An innovative degraded adhesion model for railway vehicles: development and experimental validation

E. Meli, A. Ridolfi & A. Rindi

Meccanica
An International Journal of Theoretical and Applied Mechanics AIMETA

ISSN 0025-6455
Volume 49
Number 4

Meccanica (2014) 49:919-937
DOI 10.1007/s11012-013-9839-z

Springer

Meccanica (2014) 49:919–937
DOI 10.1007/s11012-013-9839-z

An innovative degraded adhesion model for railway vehicles: development and experimental validation

E. Meli · A. Ridolfi · A. Rindi

Received: 27 May 2013 / Accepted: 7 November 2013 / Published online: 5 December 2013

Abstract The realistic description of the wheel-rail interaction is crucial in railway systems because the contact forces deeply influence the vehicle dynamics, the wear of the contact surfaces and the vehicle safety. In the modelling of the wheel-rail contact, the degraded adhesion represents a fundamental open problem. In fact an accurate adhesion model is quite hard to be developed due to the presence of external unknown contaminants (the third body) and the complex and highly non-linear behaviour of the adhesion coefficient; the problem becomes even more complicated when degraded adhesion and large sliding between the contact bodies (wheel and rail) occur.

In this work the authors describe an innovative adhesion model aimed at increasing the accuracy in reproducing degraded adhesion conditions. The new approach has to be suitable to be used inside the wheel-rail contact models usually employed in the multibody applications. Consequently the contact model, comprising the new adhesion model, has to assure both a good accuracy and a high numerical efficiency to be implemented directly online within more general vehicle multibody models (e.g. in Matlab-Simulink or Simpack environments).

The model studied in the work considers some of the main phenomena behind the degraded adhesion: the large sliding at the contact interface, the high energy dissipation, the consequent cleaning effect on the contact surfaces and, finally, the adhesion recovery due to the external unknown contaminant removal.

The new adhesion model has been validated through experimental data provided by Trenitalia S. p. A. and coming from on-track tests carried out in Velim (Czech Republic) on a straight railway track characterised by degraded adhesion conditions. The tests have been performed with the railway vehicle UIC-Z1 equipped with a fully-working Wheel Slide Protection (WSP) system.

The validation showed the good performances of the adhesion model both in terms of accuracy and in terms of numerical efficiency. In conclusion, the adhesion model highlighted the capability of well reproducing the complex phenomena behind the degraded adhesion.

Keywords Multibody modelling of railway vehicles · Wheel-rail contact · Degraded adhesion · Adhesion recovery

E. Meli (✉) · A. Ridolfi · A. Rindi
Department of Industrial Engineering, University of Florence, Via S. Marta 3, 50139 Florence, Italy
e-mail: enrico.meli@unifi.it

A. Ridolfi
e-mail: a.ridolfi@unifi.it

A. Rindi
e-mail: andrea.rindi@unifi.it

1 Introduction

The realistic description of the wheel-rail interaction is crucial in railway systems because the contact forces

deeply influence the vehicle dynamics, the wear of the contact surfaces and the vehicle safety.

Since the numerical performances (computation times and memory consumption) are very important in the multibody applications, the contact phenomena cannot be usually modelled, in practise, by considering the wheel and the rail as generic elastic continuous bodies. To overcome these limitations, the multibody contact models are generally characterised by three main logical parts: the contact point detection, the normal problem solution and the tangential problem solution, that comprises the adhesion model.

The detection of the contact point permits to calculate the contact point position on the wheel and rail surfaces. The main approaches employ either constraint equations [42, 43] or exact analytical methods aimed at the reduction of the algebraic problem dimension [9, 10, 15, 22, 23, 34]. Generally, the normal problem solution is based on the Lagrange multipliers [42, 43] and on improvements of Hertz theory [6, 11, 29]. Finally, concerning the solution of the tangential problem, different strategies have been considered in the last decades [14, 45]. The most significant approaches include the linear Kalker theory (saturated through the Johnson-Vermeulen formula) [19, 21, 28–30], the non-linear Kalker theory implemented in the FASTSIM algorithm [25–27, 29, 30, 32, 53, 54] and the Polach theory [38–41] that allows the description of the adhesion coefficient decrease with increasing creepage (excluding the spin creepage) and to well fit the experimental data. All the three steps of the contact model have to assure a good accuracy and, at the same time, a high numerical efficiency. High numerical performances are fundamental to implement the contact model directly online inside more general multibody vehicle models (developed in dedicated environments like Matlab-Simulink and Simpack), without employing discretized look-up table (LUT) [1, 2].

The main strategies employed to solve the tangential problem (comprising the adhesion model) usually do not take into account the important topic of the degraded adhesion between wheel and rail, that still remains an open problem. The substantial lack of literature characterising these issues is mainly caused by the difficulty to get a realistic adhesion law because of the presence of external unknown contaminants (the third body) and the complex and non-linear behaviour of the adhesion coefficient. The problem becomes even more complicated when degraded adhesion yields a high energy dissipation and, consequently, an adhesion recovery.

Many important analyses have been carried out over the years to investigate the role of so-called third body between the contact surfaces. More particularly the analyses have been performed both on laboratory test rigs and through on-track railway tests by considering natural and artificial external contaminants and friction modifiers [7, 8, 16, 18, 20, 24, 36, 50].

Contemporaneously, to better study the degraded adhesion non-linear behaviour, also the high energy dissipation at the contact interface and the consequent adhesion recovery have begun to be more accurately investigated [4, 5, 12, 13, 17, 33, 35, 49, 51, 52].

In this work the authors describe an innovative adhesion model aimed at increasing the accuracy in reproducing degraded adhesion conditions in multibody vehicle dynamics and railway systems. The new model, according to the recent trends of the state of the art (see the previous bibliographic references), focuses on the main phenomena behind the degraded adhesion, with particular attention to the energy dissipation at the contact interface, the consequent cleaning effect and the resulting adhesion recovery due to the removal of external unknown contaminants. Moreover, the followed approach minimises the number of hardly measurable physical quantities required by the model; this is a very important feature because most of the physical characteristics of the contaminants are totally unknown in practise.

The new model will have to assure a good accuracy to well reproduce the non-linear phenomena characterising the degraded adhesion; at the same time, it will have to guarantee high computational performances so that the whole contact model (including the adhesion model) could be implemented directly online within more general multibody models of railway vehicles.

The new adhesion model has been validated through experimental data provided by Trenitalia S. p. A. and coming from on-track tests carried out in Velim (Czech Republic) on a straight railway track characterised by degraded adhesion conditions. The tests have been performed with the railway vehicle UIC-Z1 equipped with a fully-working Wheel Slide Protection (WSP) system.

The structure of the paper is the following: the general architecture of the model will be illustrated in Sect. 2 while in Sect. 3 the multibody model, comprising the railway vehicle model and the wheel-rail contact model, will be described in detail. In Sect. 4 the

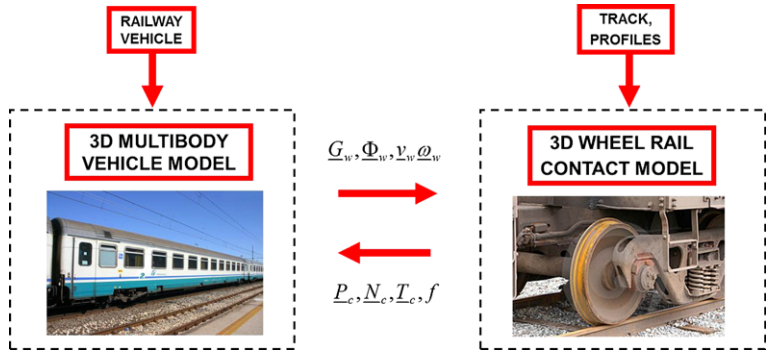

Fig. 1 Architecture of the multibody model

experimental data will be introduced and in Sects. 5, 6 and 7 the validation of the new model will be discussed. Finally conclusions and further developments will be proposed in Sect. 8.

2 General architecture of the model

The architecture of the multibody model is briefly reported in Fig. 1.

From a logical point of view, the multibody model consists of two different parts that mutually interact, directly online, during the dynamical simulation (at each integration time step): the three-dimensional (3D) model of the railway vehicle (the geometrical and physical characteristics of which are known) and the 3D wheel-rail contact model. At each time step the multibody vehicle model calculates the kinematic variables of each wheel (position $\underline{G}_w$, orientation $\underline{\Phi}_w$, velocity $\underline{v}_w$ and angular velocity $\underline{\omega}_w$) while the contact model, starting from the knowledge of these quantities, of the track geometry and of the wheel and rail profiles, evaluates the normal and tangential contact forces $\underline{N}_c$, $\underline{T}_c$ (applied to the wheel in the contact point $\underline{P}_c$) and the adhesion coefficient f, needed to carry on the dynamical simulation. Both the vehicle model and the contact model have been implemented in the Matlab-Simulink environment.

The wheel-rail contact model comprises three different steps (see Fig. 2). The detection of the contact points $\underline{P}_c$ is based on some innovative procedures recently developed by the authors in previous works [10, 22, 34]. The normal contact problem is then solved through the global Hertz theory [6, 11, 29] to evaluate the normal contact forces $\underline{N}_c$. Finally

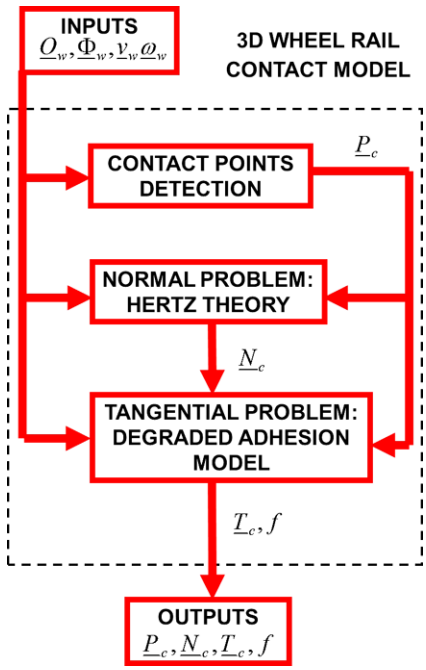

Fig. 2 Architecture of the wheel-rail contact model

the solution of the tangential contact problem is performed by means of the global Kalker-Polach theory [38–41] to compute the tangential contact forces $\underline{T}_c$ and the adhesion coefficient f.

The strategy to solve the tangential contact problem includes the innovative degraded adhesion model developed by the authors in this work (see Fig. 3). The main inputs of the degraded adhesion model are the wheel velocity $\underline{v}_w$, the wheel angular velocity $\underline{\omega}_w$, the normal force at the contact interface $\underline{N}_c$ and the position of the contact points $\underline{P}_c$. The model also requires the knowledge of some wheel-rail and contact param-

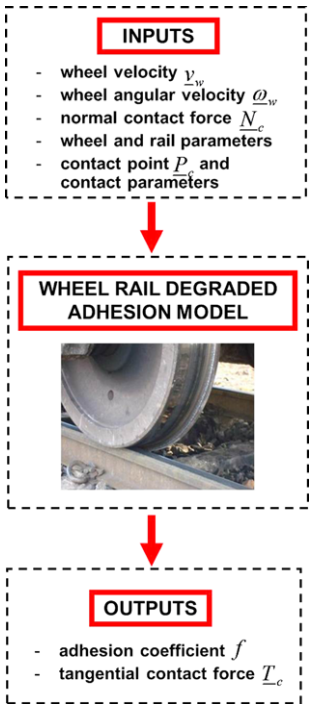

Fig. 3 Inputs and outputs of the degraded adhesion model

eters that will be introduced along the paper. The outputs of the degraded adhesion model are the desired values of the adhesion coefficient f and of the tangential contact force $\underline{T}_c$.

3 The multibody model

In this chapter the multibody model is described in detail. Firstly the 3D railway vehicle model will be analysed; secondly the attention will focus on the 3D wheel-rail contact model (comprising the contact point detection, the normal problem and the tangential problem) and, in particular, on the new degraded adhesion model.

3.1 The vehicle model

The considered railway vehicle is the UIC-Z1 wagon (illustrated in Figs. 4 and 5); its geometrical and physical characteristics are provided by Trenitalia S. p. A. [46]. The considered vehicle is equipped with a Wheel Slide Protection (WSP) system [5, 46, 48].

The wagon is composed of one carbody, two bogie frames, eight axlebox links, eight axleboxes and four wheelsets. The primary suspension, including springs and vertical dampers, connects the bogie frame to the four axleboxes while the secondary suspension, including springs, longitudinal, lateral and vertical dampers, lateral bump-stops, anti-roll bar and traction rod (the last three elements are not visible in the schematics reported in the paper), connects the carbody to the bogie frames (see Fig. 6). In Table 1 the main properties of the railway vehicle are given.

The multibody vehicle model takes into account all the degrees of freedom (DOFs) of the system bodies (one carbody, two bogie frames, eight axlebox links eight axleboxes, and four wheelsets). Consider-

Fig. 4 The UIC-Z1 wagon

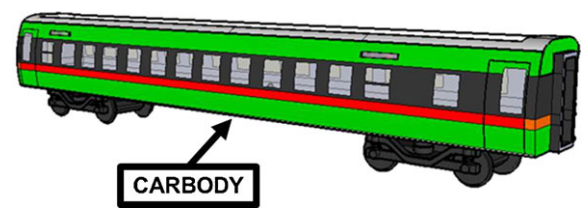

Fig. 5 Multibody vehicle model

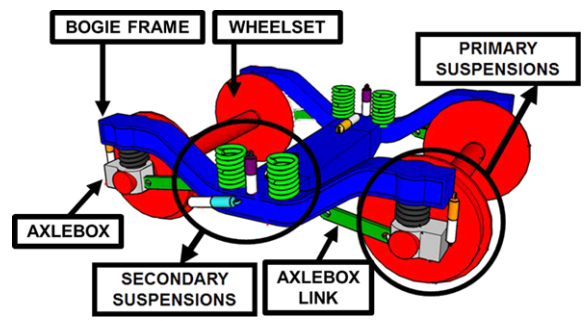

Fig. 6 Vehicle bogie

Table 1 Main characteristics of the railway vehicle

Parameter	Units	Value
Total mass	[kg]	≈43000
Wheel arrangement	–	2–2
Bogie wheelbase	[m]	2.56
Bogie distance	[m]	19
Wheel diameter	[m]	0.89
Primary suspended masses own frequency	[Hz]	≈4.5
Secondary suspended masses (carbody) own frequency	[Hz]	≈0.8

Table 2 Inertial properties of the rigid bodies

Body	Mass [kg]	I_{xx} [kg m^2]	I_{yy} [kg m^2]	I_{zz} [kg m^2]
Carbody	≈29000	76400	1494400	1467160
Bogie Frame	≈3000	2400	1900	4000
Wheelset	≈1300	800	160	800
Axlebox	≈200	3	12	12
Axlebox Link	≈60	0.5	4	4

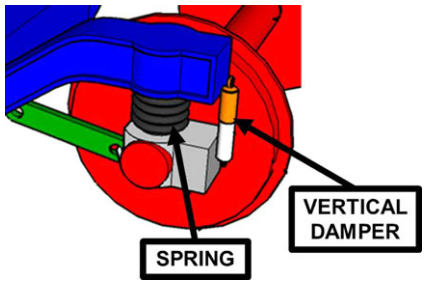

Fig. 7 Primary suspensions

ing the kinematic constraints that link to each other bogie frames, axlebox links, axleboxes and wheelsets (all cylindrical 1DOF joints) and without including the wheel-rail contacts, the whole system has 40 DOFs. The main inertial properties of the bodies are summarised in Table 2 [46].

Both the primary suspension (springs and vertical dampers) and the secondary suspension (springs, longitudinal, lateral and vertical dampers, lateral bump-stops, anti-roll bar and traction rod) have been modelled through 3D visco-elastic force elements able to describe all the main non-linearities of the system (see Figs. 6, 7 and 8).

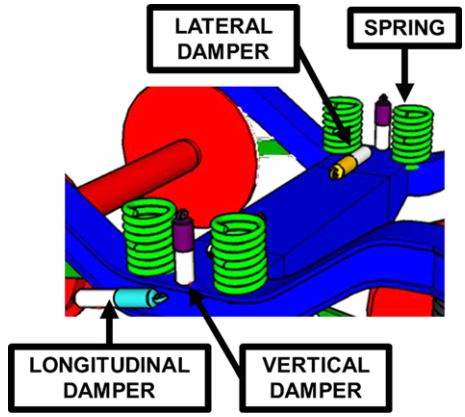

Fig. 8 Secondary suspensions

In Table 3 the characteristics of the main linear elastic force elements (springs, anti-roll bar) of both the suspension stages are reported [46]. The non-linear elastic force elements (dampers, lateral bump-stops, traction rod) have been modelled through non-linear functions that correlate the displacements and the relative velocities of the force elements connection points to the elastic and damping forces exchanged by the bodies. By way of example the non-linear characteristic of a vertical damper of the primary suspension is illustrated in Fig. 9.

The characteristics of the non-linear force elements (dampers, lateral bump-stops, traction rod) have been directly provided by Trenitalia S. p. A. More specifically, these mechanical nonlinear force elements are developed to satisfy the technical specifications required by the considered vehicle project and then experimentally tested to properly verify the desired performance [46]. Finally, also the Wheel Slide Protection (WSP) system of the railway wagon UIC-Z1 has been modelled to better investigate the vehicle behaviour during the braking phase under degraded adhesion conditions [5, 48]. The whole vehicle model has been implemented in the Matlab-Simulink environment [1].

3.2 The wheel-rail contact model

In this section the three logical parts of the wheel-rail contact model (contact point detection, normal problem and tangential problem) will be analysed with particular regard to the new degraded adhesion model. The model inputs are the kinematic variables of each wheel (position $\underline{G}_w$, orientation $\underline{\Phi}_w$, velocity $\underline{v}_w$ and

Table 3 Main linear elastic characteristics of the two stage suspensions

Element	Transl. stiff. x [N/m]	Transl. stiff. y [N/m]	Transl. stiff. z [N/m]	Rotat. stiff. x [N m/rad]	Rotat. stiff. y [N m/rad]	Rotat. stiff. z [N m/rad]
Springs of the primary suspension	844000	844000	790000	10700	10700	0
Springs of the secondary suspension	124000	124000	340000	0	0	0
Anti-roll bar	0	0	0	2.5×10^6	0	0

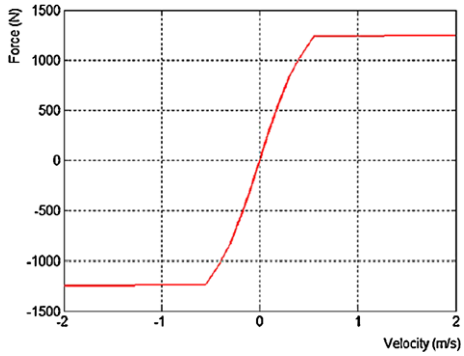

Fig. 9 Example of non-linear characteristic: vertical damper of the primary suspension

angular velocity $\underline{\omega}_w$) together with the track geometry and the wheel and rail profiles while the outputs the normal and tangential contact forces $\underline{N}_c$, $\underline{T}_c$ (applied to the wheel in the contact point $\underline{P}_c$) and the adhesion coefficient f.

3.2.1 The contact point detection

Referring to Fig. 2 the contact point detection algorithm allows the calculation of the contact points $\underline{P}_c$ starting from the wheel position $\underline{G}_w$ and orientation $\underline{\Phi}_w$, the track geometry and the wheel and rail profiles. The detection procedure has been developed by the authors in previous works [10, 22, 34] and is based on the reduction of the algebraic problem dimension through exact analytical techniques; this reduction represents the main feature of the new algorithm. The main characteristics of the innovative procedure can be summarised as follows:

- it is a fully 3D algorithm that takes into account all the six relative DOFs between wheel and rail;
- it is able to support generic railway tracks and generic wheel and rail profiles;
- it assures a general and accurate treatment of the multiple contact without introducing simplifying assumptions on the problem geometry and kinematics and limits on the number of contact points detected;
- it assures high numerical efficiency making possible the online implementation within the commercial multibody software (like Simpack Rail and Adams Rail) without discrete LUT [1, 2].

The contact point position can be evaluated imposing the following parallelism conditions [15]:

$$\begin{aligned} &\underline{n}_r^r\left(\underline{P}_r^r\right) \times \underline{n}_w^r\left(\underline{P}_w^r\right) = \underline{n}_r^r\left(\underline{P}_r^r\right) \times R_w^r \underline{n}_w^w\left(\underline{P}_w^w\right) = \underline{0} \\ &\underline{n}_r^r\left(\underline{P}_r^r\right) \times \underline{d}^r = \underline{0} \end{aligned} \tag{1}$$

where

$$\begin{aligned} &\underline{P}_w^w(x_w, y_w) = \left(x_w \;\; y_w \;\; -\sqrt{w(y_w)^2 - x_w^2}\right)^T \\ &\underline{P}_r^r(x_r, y_r) = \left(x_r \;\; y_r \;\; r(y_r)\right)^T \end{aligned} \tag{2}$$

are the positions of the generic points on the wheel surface and on the rail surface (expressed in the reference systems $G_w x_w y_w z_w$ and $O_r x_r y_r z_r$), $w(y_w)$ and $r(y_r)$ are the wheel and rail profiles (supposed to be known), $\underline{n}_w^w$ and $\underline{n}_r^r$ are the outgoing normal unit vectors to the wheel and rail surfaces (in the reference systems $G_w x_w y_w z_w$ and $O_r x_r y_r z_r$), R_w^r is the rotation matrix that links the reference system $G_w x_w y_w z_w$ to the reference system $O_r x_r y_r z_r$ and $\underline{d}^r$ is the distance vector between two generic points on the wheel surface and on the rail surface (both referred to the reference system $O_r x_r y_r z_r$): $\underline{d}^r(x_w, y_w, x_r, y_r) = \underline{P}_w^r(x_w, y_w) - \underline{P}_r^r(x_r, y_r)$ in which $\underline{P}_w^r = \underline{O}_w^r + R_w^r \underline{P}_w^w(x_w, y_w)$ is the position of the generic point of the wheel surface expressed in the reference system $O_r x_r y_r z_r$ (see Fig. 10).

The first condition of the system (1) imposes the parallelism between the normal unit vectors, while the second one requires the parallelism between the normal unit vector to the rail surface and the distance vector. The system (1) consists of six non-linear equations in the unknowns (x_w, y_w, x_r, y_r) (only four equations are independent and therefore the problem is 4D).

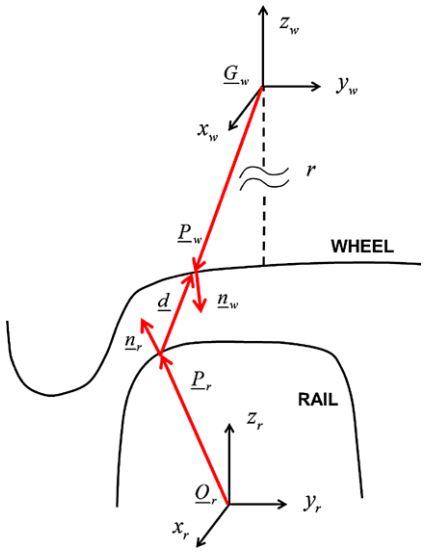

Fig. 10 Wheel-rail contact point detection

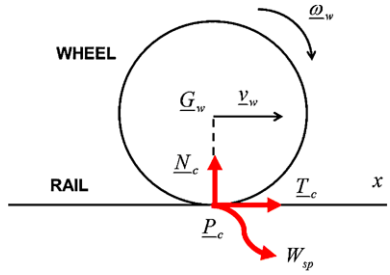

Fig. 11 Contact forces

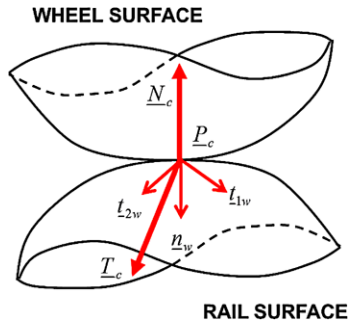

Fig. 12 Contact surfaces

However it is possible to exactly express three of the four variables (in this case (x_w, x_r, y_r)) as a function of y_w, reducing the original 4D problem to a single 1D scalar equation in the variable y_w [10, 22, 34]:

$$F(y_w) = 0. \tag{3}$$

At this point the simple scalar Eq. (3) can be easily solved through appropriate numerical algorithms. Finally, once obtained the generic solution y_{wc} of Eq. (3), the complete solution $(x_{wc}, y_{wc}, x_{rc}, y_{rc})$ of the system (1) and consequently the contact points $\underline{P}^r_{wc} = \underline{P}^r_w(x_{wc}, y_{wc})$ and $\underline{P}^r_{rc} = \underline{P}^r_r(x_{rc}, y_{rc})$ can be found by substitution.

3.2.2 *The normal contact problem*

Starting from the kinematic variables of the wheel and the contact point position $\underline{P}_c$, the normal forces $\underline{N}_c$ are calculated through the global Hertz theory for each contact point (see the Figs. 2, 10, 11 and 12) [6, 10, 11, 29]:

$$\underline{N}_c = N_c \underline{n}_w, \qquad N_c = \|\underline{N}_c\|. \tag{4}$$

The main physical hypotheses behind the Hertz global theory are the following [6, 10, 11, 29]:

– linear elasticity;
– contact patch dimensions small if compared to the curvature radii of the contact bodies surfaces;
– not-conformal contact;
– elliptic contact area.

The scalar value N_c of $\underline{N}_c$ can be evaluated as follows:

$$N_c = \left[-k_h |p_n|^\gamma + k_v |v_n| \frac{\text{sign}(v_n) - 1}{2}\right] \times \frac{\text{sign}(p_n) - 1}{2} \tag{5}$$

where $p_n = \max(\underline{d}^r \cdot \underline{n}^r_w, 0)$ is the normal penetration, γ is the Hertz's exponent equal to $3/2$, k_v is the contact damping constant, $v_n = \underline{V}_c \cdot \underline{n}^r_r$ is the normal penetration velocity ($\underline{V} = \underline{v}_w + \underline{\omega}_w \times (\underline{P}_c - \underline{G}_w)$ is the velocity of the contact point rigidly connected to the wheel). The quantity k_h is the Hertzian constant, function both of the material properties (the Young modulus E, the shear modulus G and the Poisson coefficient σ) and of the contact bodies geometry through the curvatures of the contact surfaces (easily computable if the contact point position $\underline{P}_c$ is known).

Finally it is worth noting that the Hertz theory allows also the calculation of the semi-axes a and b of the elliptical contact patch, depending on the material properties, the curvatures of the contact surfaces and the normal contact force N_c (or, equivalently, the normal penetration p_n) [6, 10, 11, 29].

3.2.3 The tangential contact problem and the degraded adhesion model

In this section the tangential contact forces $\underline{T}_c$ and the adhesion coefficient f will be calculated solving the tangential contact problem [38–41]. Particularly the attention will focus on the new adhesion model especially developed for degraded adhesion conditions. The inputs of the model are kinematic variables of the wheel (position $\underline{G}_w$, orientation $\underline{\Phi}_w$, velocity $\underline{v}_w$ and angular velocity $\underline{\omega}_w$), the contact point position $\underline{P}_c$ and the normal contact forces $\underline{N}_c$ (see the Figs. 2, 3, 10, 11 and 12).

In this case the main hypotheses behind the Kalker-Polach global theory, on which the new adhesion model is based, can be summarised as follows [38–41]:

- linear proportionality between tangential displacements and tangential stresses;
- subdivision of the contact patch into adhesion area and slip area;
- constant friction coefficient inside the contact patch.

The global Hertz and Kalker-Polach theories are usually employed in the railway field because they permit to study most of the interesting physical cases and represent a very good compromise between accuracy and numerical efficiency in this research area.

With regard to Figs. 11 and 12, for each contact point $\underline{P}_c$, it is possible to determine the sliding $\underline{s}$ (with its longitudinal and lateral components s_x, s_y):

$$\begin{aligned} &\underline{s} = \underline{v}_w + \underline{\omega}_w \times (\underline{P}_c - \underline{G}_w) \\ &s = \|\underline{s}\|, \qquad s_x = \underline{s} \cdot \underline{t}_{1w}, \qquad s_y = \underline{s} \cdot \underline{t}_{2w} \end{aligned} \tag{6}$$

where $\underline{n}_w$, $\underline{t}_{1w}$ and $\underline{t}_{1w}$ are respectively the normal unit vector and the tangential unit vectors (in longitudinal and lateral direction) corresponding to the generic contact point $\underline{P}_c$ (see Fig. 12). Subsequently the creepage $\underline{e}$ can be introduced

$$\begin{aligned} &\underline{e} = \frac{\underline{s}}{v_w}, \qquad v_w = \|\underline{v}_w\| \\ &e_x = \underline{e} \cdot \underline{t}_{1w}, \qquad e_y = \underline{e} \cdot \underline{t}_{2w} \end{aligned} \tag{7}$$

together with the adhesion coefficient f and the specific dissipated energy W_{sp} at the contact area:

$$\begin{aligned} &e = \|\underline{e}\|, \qquad T_c = \|\underline{T}_c\| \\ &T_x = \underline{T}_c \cdot \underline{t}_{1w} = T_c \frac{e_x}{e}, \qquad T_y = \underline{T}_c \cdot \underline{t}_{2w} = T_c \frac{e_y}{e} \\ &f = \frac{T_c}{N_c}, \qquad W_{sp} = \underline{T}_c \cdot \underline{e} = T_c e = f N_c e \end{aligned} \tag{8}$$

in this way the specific dissipated energy W_{sp} can also be interpreted as the energy dissipated at the contact for unit of distance travelled by the railway vehicle (see Eqs. (7) and (8)).

The main phenomena characterising the degraded adhesion are the large sliding occurring at the contact interface and, consequently, the high energy dissipation. Such a dissipation causes a cleaning effect on the contact surfaces and finally an adhesion recovery due to the removal of external contaminants. When the specific dissipated energy W_{sp} is low the cleaning effect is almost absent, the contaminant level h does not change and the adhesion coefficient f is equal to its original value in degraded adhesion conditions f_d. As the energy W_{sp} increases, the cleaning effect increases too, the contaminant level h becomes thinner and the adhesion coefficient f raises. In the end, for large values of W_{sp}, all the contaminant is removed (h is null) and the adhesion coefficient f reaches its maximum value f_r; the adhesion recovery due to the removal of external contaminants is now completed. At the same time if the energy dissipation begins to decrease, due for example to a lower sliding, the reverse process occurs (see Figs. 13 and 14).

Since the contaminant level h and its characteristics are usually totally unknown, it is useful trying to experimentally correlate the adhesion coefficient f directly with the specific dissipated energy W_{sp} (see Eq. (8)). To reproduce the qualitative trend previously described and to allow the adhesion coefficient to vary between the extreme values f_d and f_r, the following expression for f is proposed:

$$f = \big[1 - \lambda(W_{sp})\big] f_d + \lambda(W_{sp}) f_r \tag{9}$$

where $\lambda(W_{sp})$ is an unknown transition function between degraded adhesion and adhesion recovery. The function $\lambda(W_{sp})$ has to be positive and monotonous increasing; moreover the following boundary conditions are supposed to be verified: $\lambda(0) = 0$ and $\lambda(+\infty) = 1$.

This way the authors suppose that the transition between degraded adhesion and adhesion recovery only depends on W_{sp}. This hypothesis is obviously only an approximation but, as it will be clearer in the next chapters, it well describes the adhesion behaviour. Initially, to catch the physical essence of the problem without introducing a large number of unmanageable and unmeasurable parameters, the authors have chosen the following simple expression for $\lambda(W_{sp})$:

$$\lambda(W_{sp}) = 1 - e^{-\tau W_{sp}} \tag{10}$$

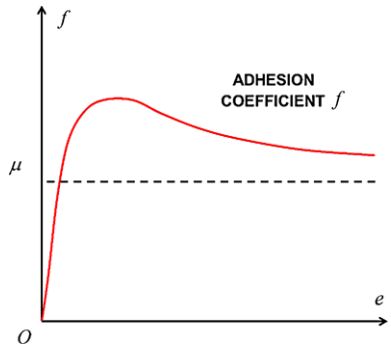

Fig. 13 Standard behaviour of the adhesion coefficient f

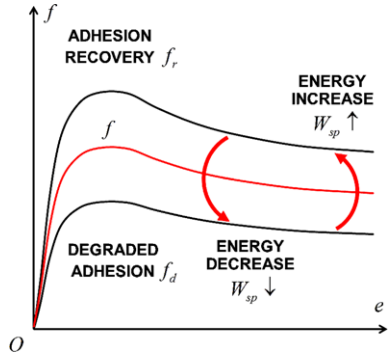

Fig. 14 The adhesion coefficient f and the specific dissipated energy W_{sp} under degraded adhesion conditions

where τ is now the only unknown parameter to be tuned on the base of the experimental data.

At this step of the research activity, the analytical transition function $\lambda(W_{sp})$ has been thought to describe in the best possible way the asymptotic transition from degraded adhesion (low dissipated energy) to full adhesion recovery (high dissipated energy). In particular, the choice of function and boundary conditions has been inspired by the asymptotic behaviour of the experimental transition function $\lambda^{sp}(W_{sp}^{sp})$ (clearly visible in the Figs. 18, 19, 20 of Sect. 5.1 and Figs. 24, 25, 26 of Sect. 5.2).

Concerning the choice of the specific transition function, there are different possible functions (obviously satisfying the previous boundary conditions) to correctly approximate the experimental data. In this circumstance, an exponential function seems to reproduce in a very natural way the qualitative behaviour of the experimental transition function $\lambda^{sp}(W_{sp}^{sp})$. Moreover the chosen function is very simple: it is characterised by only one unknown parameter and, consequently, it is very easy to be tuned. This is a fundamental feature because a larger number of unknown parameters would make the model more difficult to be tuned and validated and more depending on the specific considered scenario.

In this research activity the two main adhesion coefficients f_d and f_r (degraded adhesion and adhesion recovery) have been calculated according to Polach [29, 38, 39]:

$$\begin{aligned} f_d &= \frac{2\mu_d}{\pi}\left[\frac{k_{ad}\varepsilon_d}{1+(k_{ad}\varepsilon_d)^2} + \operatorname{arctg}(k_{sd}\varepsilon_d)\right] \\ f_r &= \frac{2\mu_r}{\pi}\left[\frac{k_{ar}\varepsilon_r}{1+(k_{ar}\varepsilon_r)^2} + \operatorname{arctg}(k_{sr}\varepsilon_r)\right] \end{aligned} \tag{11}$$

where

$$\varepsilon_d = \frac{2}{3}\frac{C\pi a^2 b}{\mu_d N_c}e, \qquad \varepsilon_r = \frac{2}{3}\frac{C\pi a^2 b}{\mu_r N_c}e. \tag{12}$$

The quantities k_{ad}, k_{sd} and k_{ar}, k_{sr} are the Polach reduction factors (for degraded adhesion and adhesion recovery respectively) and μ_d, μ_r are the friction coefficient defined as follows

$$\begin{aligned} \mu_d &= \left(\frac{\mu_{cd}}{A_d} - \mu_{cd}\right)e^{-\gamma_d s} + \mu_{cd} \\ \mu_r &= \left(\frac{\mu_{cr}}{A_r} - \mu_{cr}\right)e^{-\gamma_r s} + \mu_{cr} \end{aligned} \tag{13}$$

in which μ_{cd}, μ_{cr} are the kinetic friction coefficients, A_d, A_r are the ratios between the kinetic friction coefficients and the static ones and γ_d, γ_d are the friction decrease rates. The Polach approach (see Eq. (11)) has been followed since it permits to describe the decrease of the adhesion coefficient with increasing creepage and to better fit the experimental data (see Figs. 13 and 14).

Finally it has to be noticed that the semi-axes a and b of the contact patch (see Eq. (12)) depend only on the material properties, the contact point position P_c on wheel and rail (through the curvatures of the contact surfaces in the contact point) and the normal force N_c, while the contact shear stiffness C (N/m^3) is a function only of material properties, the contact patch semi-axes a and b and the creepages. More particularly, the following relation holds [29]:

$$C = \frac{3G}{8a}\sqrt{\left(c_{11}\frac{e_x}{e}\right)^2 + \left(c_{22}\frac{e_y}{e}\right)^2} \tag{14}$$

where $c_{11} = c_{11}(\sigma, a/b)$ and $c_{22} = c_{22}(\sigma, a/b)$ are the Kalker coefficients.

In the end, the desired values of the adhesion coefficient f and of the tangential contact force $T_c = fN_c$

can be evaluated by solving the algebraic Eq. (9) in which the explicit expression of W_{sp} has been inserted (see Eq. (8)):

$$f = \Im(f, t) \tag{15}$$

where $\Im$ indicates the generic functional dependence. Due to the simplicity of the transition function $\lambda(W_{sp})$, the solution can be easily obtained through standard non-linear solvers [31]. From a computational point of view, the adhesion coefficient f_i can be computed at each integration time t_i as follows

$$f_i = \Im(f_i, t_i). \tag{16}$$

Eventually, the vector tangential contact force $\underline{T}_c$ has to be calculated. To this aim the creepage $\underline{e}$ can be employed:

$$\begin{aligned} &T_x = T_c \frac{e_x}{e}, \qquad T_y = T_c \frac{e_y}{e} \\ &\underline{T}_c = T_x \underline{t}_{w1} + T_y \underline{t}_{w2}. \end{aligned} \tag{17}$$

In this phase of the research activity concerning the degraded adhesion, the contact spin at the wheel-rail interface has not been considered. The components of the spin moment $\underline{M}_{sp} = M_{sp}\underline{n}_w$ produced by the spin creepage $e_{sp} = \underline{\omega}_w \cdot \underline{n}_w / v_w$ and by the lateral creepage e_y can be neglected because they are quite small. On the other hand the effect of the spin creepage e_{sp} on the lateral contact force T_y may be not negligible. This limitation can be partially overcome thanks to the Polach theory [38, 39] that takes into account, in an approximated way, the effect of the spin creepage on the lateral contact force T_{sp}:

$$\begin{aligned} T_x &= T_c' \frac{e_x}{e_m} \\ T_y &= T_c' \frac{e_y}{e_m} + T_{sp} \frac{e_{sp}}{e_m} \end{aligned} \tag{18}$$

where e_m is the modulus of the modified translational creepage $\underline{e}_m$, T_{sp} is the lateral contact force caused by the spin creepage e_{sp} and T_c' is the modulus of the old tangential contact force calculated before. The quantities T_{sp} and $\underline{e}_m$ are evaluated in [38] starting from the geometrical and physical characteristics of the system; however T_{sp}, differently from T_c', does not consider the decrease of the adhesion coefficient with increasing creepage and the adhesion recovery under degraded adhesion conditions introduced by the authors.

More in general, the role of the contact spin under degraded adhesion conditions, especially in presence of adhesion recovery, is still an open problem.

Table 4 Main wheel, rail and contact parameters

Parameter	Units	Value
Young modulus	[Pa]	2.1×10^{11}
Shear modulus	[Pa]	8.0×10^{10}
Poisson coefficient	[N s/m]	0.3
Contact damping constant	–	1.0×10^{5}
Polach reduction factor k_{ad}	–	0.3
Polach reduction factor k_{sd}	–	0.1
Polach reduction factor k_{ar}	–	1.0
Polach reduction factor k_{sr}	–	0.4
Kinetic friction coefficient μ_{cd}	–	0.06
Kinetic friction coefficient μ_{cr}	–	0.28
Friction ratio A_d	–	0.40
Friction ratio A_r	–	0.40
Friction decrease rate γ_d	[s/m]	0.20
Friction decrease rate γ_r	[s/m]	0.60

4 The experimental data

The degraded adhesion model has been validated by means of experimental data [47], provided by Trenitalia S. p. A., coming from on-track tests performed in Velim (Czech Republic) with the coach UIC-Z1 (see Figs. 4 and 5). The considered vehicle is equipped with a fully-working Wheel Slide Protection (WSP) system [46, 48].

The experimental tests have been carried out on a straight railway track. The wheel profile is the ORE S1002 (with a wheelset width d_w equal to 1.5 m and a wheel radius r equal to 0.445 m) while the rail profile is the UIC60 (with a gauge d_r equal to 1.435 m and a laying angle equal to 1/20 rad). In Table 4 the main wheel, rail and contact parameters are reported [3, 38, 39].

The value of the kinetic friction coefficient under degraded adhesion conditions μ_{cd} depends on the test performed on the track; the degraded adhesion conditions are usually reproduced using a watery solution containing surface-active agents, e.g. a solution sprinkled by a specially provided nozzle directly on the wheel-rail interface on the first wheelset in the running direction. The surface-active agent concentration in the solution varies according to the type of test and the desired friction level. The value of the kinetic friction coefficient under full adhesion recovery μ_{cs} corresponds to the classical kinetic friction coefficient under dry conditions.

Table 5 Test initial velocities

Initial velocities	Units	Value
Group A, I test	[m/s]	42.3
Group A, II test	[m/s]	40.4
Group A, III test	[m/s]	40.8
Group B, I test	[m/s]	40.8
Group B, II test	[m/s]	41.1
Group B, III test	[m/s]	41.8

During the experimental campaign six different braking tests have been performed. The six tests have been split into two groups (A and B): the first group has been used to tune the degraded adhesion model (in particular the unknown parameter τ, see Sect. 3.2.3, Eq. (10)) while the second one to properly validate the tuned model. The initial vehicle velocities corresponding to the considered tests are reported in Table 5.

For each test the following physical quantities have been experimentally measured (with a sample time Δt_s equal to 0.01 s):

- the longitudinal vehicle velocity v_v^{sp}. For the sake of simplicity all the longitudinal wheel velocities v_{wj}^{sp} (j represents the j-th wheel) are considered equal to v_v^{sp}. The acceleration of the vehicle a_v^{sp} and of the wheels a_{wj}^{sp} can be obtained by derivation and by properly filtering the numerical noise.
- the rotation velocities of all the wheels ω_{wj}^{sp}.
- the vertical loads N_{wj}^{sp} on the wheels. The vertical contact forces N_{cj}^{sp} can be approximately evaluated starting from N_{wj}^{sp} by taking into account the weight of the wheels. Also in this case the angular accelerations $\dot{\omega}_{wj}^{sp}$ can be calculated by derivation and by properly filtering.
- the traction or braking torques C_{wj}^{sp} applied to the wheels.

By way of example in Fig. 15 the wheel translational and rotational velocities v_{w1}^{sp} and $r\omega_{w1}^{sp}$ are reported for the I test of the group A; both the WSP intervention and the adhesion recovery in the second part of the braking manoeuvre are clearly visible.

On the base of the measured data, the experimental outputs of the degraded adhesion model, e.g. the adhesion coefficient f_j^{sp}, the tangential contact force T_{cj}^{sp} and the transition function λ_j^{sp} have now to be computed for all the tests. These experimental quantities are fundamental for the validation both of the degraded

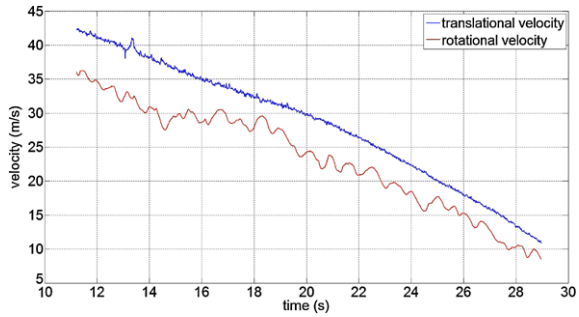

Fig. 15 Wheel translational and rotational velocities v_{w1}^{sp} and $r\omega_{w1}^{sp}$ for the I test of the group A

adhesion model (Sect. 5) and of the whole multibody model (Sect. 6). To reach this goal and to effectively exploit the measured data, in this phase the wheelset is supposed to be placed in its centred position; in this way the position of the single contact point P_c can be supposed to be known and nearly constant and the surface curvatures in the contact points, the semi-axes of the contact patch a, b and the contact shear stiffness C can be easily calculated [29]. Moreover the following simplified expressions for the sliding s_j^{sp}, for the creepage e_j^{sp} and for C hold:

$$s_j^{sp} = v_{wj}^{sp} - r\omega_{wj}^{sp}, \qquad e_j^{sp} = \frac{s_j^{sp}}{v_{wj}^{sp}}$$
$$C = \frac{3Gc_{11}}{8a}. \tag{19}$$

Starting from s_j^{sp} and e_j^{sp}, T_{cj}^{sp} can be estimated through the rotational equilibrium of the wheel with respect to the origin G_w:

$$J_w\dot{\omega}_{wj}^{sp} = C_{wj}^{sp} - rT_{cj}^{sp} \tag{20}$$

in which $J_w = 160\ \mathrm{kg\,m^2}$ is the wheel inertia. Subsequently Eq. (8) permits to calculate f_j^{sp} and the specific dissipation energy W_{spj}^{sp} while f_{dj}^{sp}, f_{rj}^{sp} can be computed directly through Eq. (11). Finally, from the knowledge of W_{spj}^{sp} and f_j^{sp}, f_{dj}^{sp}, f_{rj}^{sp}, the trend of the experimental transition function $\lambda_j^{sp}(W_{spj}^{sp})$ can be determined by means of Eq. (9). For instance in Fig. 16 the adhesion coefficient f_1^{sp} and its limit values f_{d1}^{sp}, f_{r1}^{sp} under degraded adhesion and adhesion recovery are illustrated always for the I test of the group A (the adhesion recovery in the second part of the braking manoeuvre is clear). Figure 17 shows the experimental trend of the transition function λ_1^{sp}.

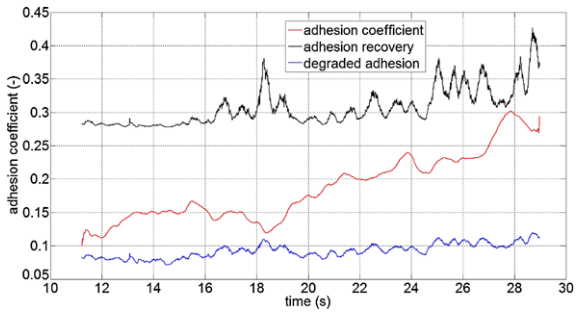

Fig. 16 Adhesion coefficient f_1^{sp} and its limit values f_{d1}^{sp}, f_{r1}^{sp} for the I test of the group A

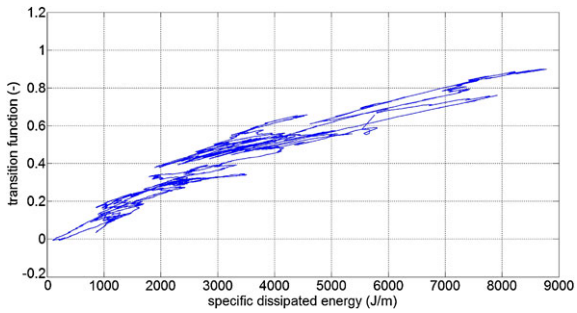

Fig. 17 Experimental transition function $\lambda_1^{sp}(W_{sp1}^{sp})$ for the I test of the group A

5 Tuning and validation of the degraded adhesion model

In this chapter the tuning and the validation of the degraded adhesion model will be described. Both the tuning and the validation will be performed without considering the complete vehicle dynamics that, on the contrary, will be taken into account in the Sect. 6.

5.1 Model tuning

During this phase of the research activity, the degraded adhesion model has been tuned on the base of the three experimental braking tests of the group A. In particular the attention focused on the transition function $\lambda(W_{sp})$ and on the τ parameter. Starting from the experimental transition functions $\lambda_j^{sp}(W_{spj}^{sp})$ corresponding to the three tests of the group A, the parameter τ within $\lambda(W_{sp})$ has been tuned through a Non-linear Least Square Optimisation (NLSO) by minimising the

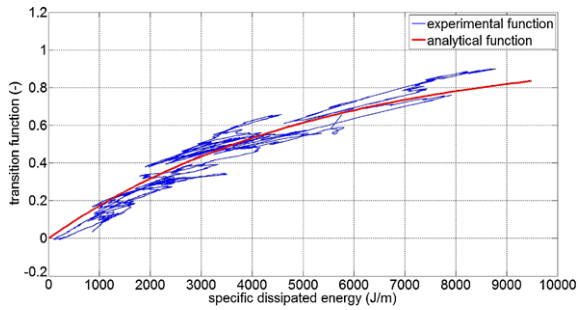

Fig. 18 Comparison between $\lambda(W_{sp})$ and $\lambda_1^{sp}(W_{sp1}^{sp})$ for the I test of the group A

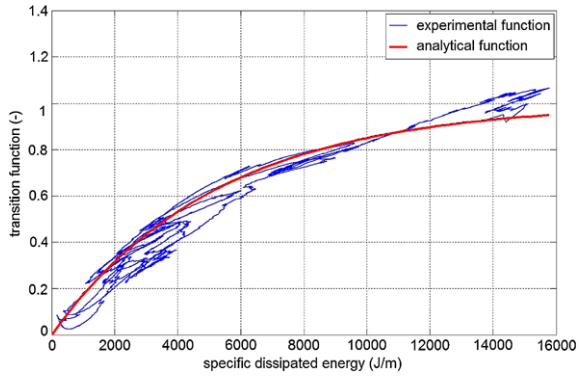

Fig. 19 Comparison between $\lambda(W_{sp})$ and $\lambda_1^{sp}(W_{sp1}^{sp})$ for the II test of the group A

following error function [1, 31, 37]:

$$g(\tau) = \sum_{k=1}^{3} \sum_{i=1}^{N_t} \sum_{j=1}^{N_w} \left[\lambda_{jk}^{sp}\left(W_{jk}^{sp}(t_i)\right) - \lambda\left(W_{jk}^{sp}(t_i)\right)\right]^2 \tag{21}$$

where N_w is the wheel number and N_t is the measured sample number; this time the index k indicates the k-th test of the group A. In this case the optimisation process provided the optimum value $\tau = 1.9 \times 10^{-4}$ m/J. For instance the comparisons between the optimised analytical transition function $\lambda(W_{sp})$ and the experimental transition function $\lambda_1^{sp}(W_{sp1}^{sp})$ are shown for the three tests of the group A in Figs. 18, 19 and 20.

Subsequently, always for the tests of the group A, the adhesion coefficient f_j has been calculated according to Sect. 3.2.3 by means of Eq. (16) starting from the knowledge of the experimental inputs v_{wj}^{sp}, ω_{wj}^{sp} and N_{cj}^{sp}; as in Sect. 4, the simplified relations of Eq. (19) have been employed. In this circumstance the optimised analytical transition function $\lambda(W_{sp})$

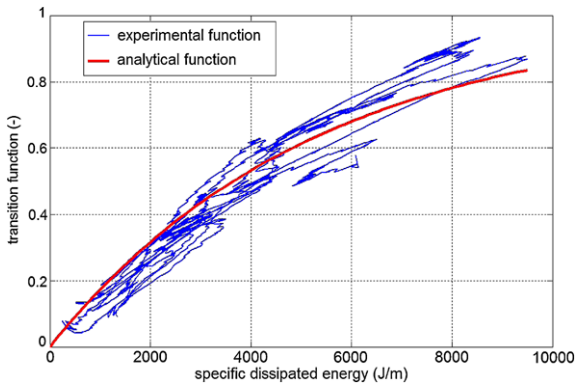

Fig. 20 Comparison between $\lambda(W_{sp})$ and $\lambda_1^{sp}(W_{sp1}^{sp})$ for the III test of the group A

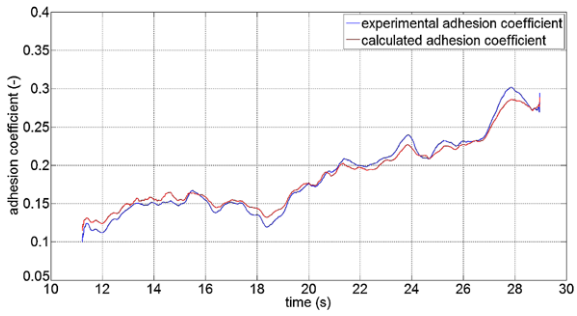

Fig. 21 Comparison between f_1 and f_1^{sp} for the I test of the group A

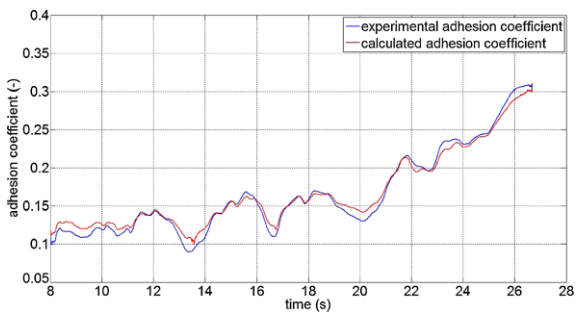

Fig. 22 Comparison between f_1 and f_1^{sp} for the II test of the group A

has been used. The behaviour of the calculated adhesion coefficient f_j has been compared with the experimental one f_j^{sp} (see Sect. 4). By way of example, in Figs. 21, 22, 23 the time histories of f_1 and f_1^{sp} are reported for all the tests of the group A.

The results of the tuning process highlight the good capability of the simple analytical transition function, $\lambda(W_{sp})$ in reproducing the experimental trend of

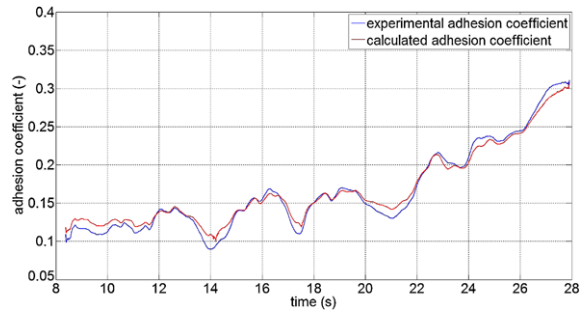

Fig. 23 Comparison between f_1 and f_1^{sp} for the III test of the group A

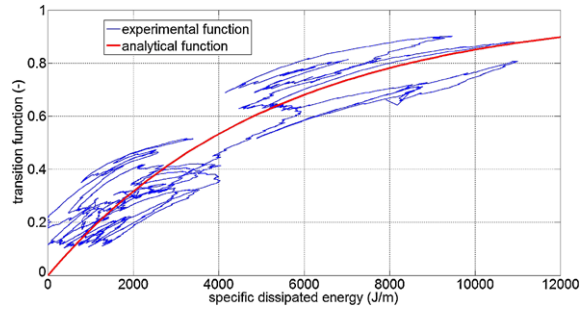

Fig. 24 Comparison between $\lambda(W_{sp})$ and $\lambda_1^{sp}(W_{sp1}^{sp})$ for the I test of the group B

$\lambda_j^{sp}(W_{spj}^{sp})$ for all the tests of the group A. The good behaviour of the analytical transition function despite its simplicity (only one unknown parameter is involved), allows also a good matching of the experimental data in terms of the adhesion coefficient (see the trend of f_j and f_j^{sp} and the adhesion recovery in the second part of the braking manoeuvre).

5.2 Model validation

The real validation of the degraded adhesion model has been carried out by means of the three experimental braking tests of the group B. Also in this case the attention focused, first of all, on the analytical transition function $\lambda(W_{sp})$ (the same tuned in Sect. 5.1 with $\tau = 1.9 \times 10^{-4}$ m/J) and on its capability in matching the behaviour of the experimental transition functions $\lambda_j^{sp}(W_{spj}^{sp})$. The comparison between $\lambda(W_{sp})$ and $\lambda_1^{sp}(W_{sp1}^{sp})$ is illustrated in Figs. 24, 25, 26 for the tests of the group B.

Similarly to Sect. 5.1 the adhesion coefficient f_j has been calculated for the tests of the group B (see Sect. 3.2.3 and Eq. (16)) starting from the knowledge

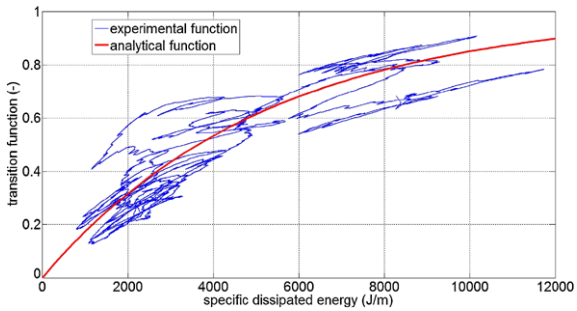

Fig. 25 Comparison between $\lambda(W_{sp})$ and $\lambda_1^{sp}(W_{sp1}^{sp})$ for the II test of the group B

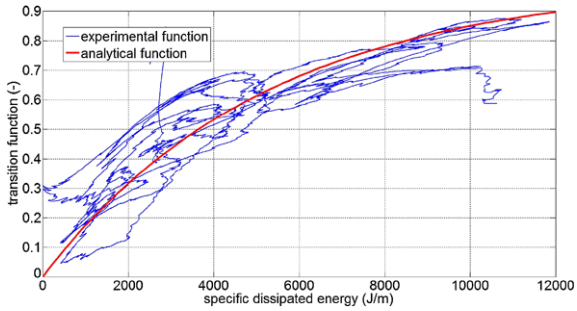

Fig. 26 Comparison between $\lambda(W_{sp})$ and $\lambda_1^{sp}(W_{sp1}^{sp})$ for the III test of the group B

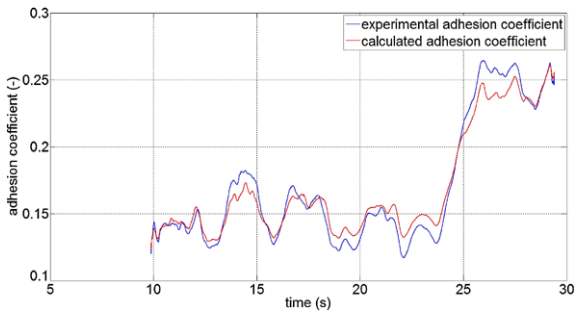

Fig. 27 Comparison between f_1 and f_1^{sp} for the I test of the group B

of the experimental inputs v_{wj}^{sp}, ω_{wj}^{sp} and N_{cj}^{sp} (the simplified relations of Eq. (19) in Sect. 4 have been used). Obviously, the same analytical transition function $\lambda(W_{sp})$ optimised in Sect. 5.1 has been employed. The behaviour of the calculated adhesion coefficient f_j and the experimental one f_j^{sp} (see Sect. 4) have been compared again. For instance in Figs. 27, 28, 29 the time histories of f_1 and f_1^{sp} are reported for all the tests of the group B.

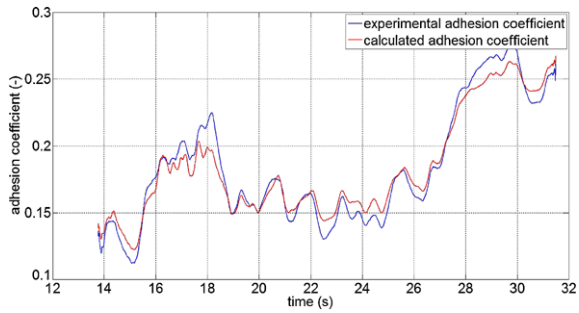

Fig. 28 Comparison between f_1 and f_1^{sp} for the II test of the group B

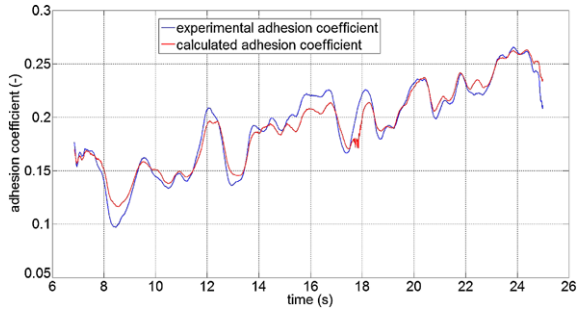

Fig. 29 Comparison between f_1 and f_1^{sp} for the III test of the group B

The results of the model validation are encouraging and highlight the good matching between the analytical transition function $\lambda(W_{sp})$ (tuned in Sect. 5.1 on the base of the tests of the group A) and the new experimental data $\lambda_j^{sp}(W_{spj}^{sp})$ corresponding to the tests of the group B. At the same time, also for the group B, there is a good correspondence between the time histories of the calculated adhesion coefficient f_j and those of the experimental one f_j^{sp} (see the adhesion recovery in the second part of the braking manoeuvre). The satisfying results obtained for the validation group B confirm the capability of the simple analytical transition function $\lambda(W_{sp})$ in approximating the complex and highly non-linear behaviour of the degraded adhesion.

Moreover the new degraded adhesion model present two important advantages. Firstly, it only introduces one additional parameter (e.g. the τ rate), very easy to be experimentally tuned, without requiring the knowledge of further unknown physical properties of the contaminant. Secondly, the model guarantees a very low computational load, making possible the on-line implementation of the procedure within more gen-

eral multibody models built in dedicated environments [1, 2].

On the other hand, at this phase of the research activity, the adhesion model is characterised by two main limitations:

- the limitedness of the experimental campaign (needed for the model tuning and validation), especially in terms of analysed scenarios (in this case braking on straight track under degraded adhesion conditions). Anyway the two different sets of experimental tests employed in this work for the model tuning and validation are completely independent. This confirms the accuracy of the model in reproducing the complex system behaviour despite the criticality of the considered scenario and the nonlinearity and the chaoticity of the phenomenon;
- the considered transition function $\lambda(W_{sp})$ (that is the relation between the adhesion coefficient f and the specific dissipated energy W_{sp}) is based on the fitting of experimental data and not on more elementary physical phenomena.

The next steps of the research will be fundamental to overcome the previous limitations and to better investigate the degraded adhesion from a physical viewpoint (see Sect. 8).

6 The validation of the whole multibody model

In this chapter the behaviour of the complete multibody model described in Sect. 3 will be analysed. The vehicle dynamic analysis is focused on the translation and rotational wheel velocities v_{wj}, $r\omega_{wj}$ corresponding to the tests of the tuning group A and the validation group B; more precisely, in this case v_{wj} is the longitudinal component of $\underline{v}_{wj}$, ω_{wj} is the component of $\underline{\omega}_{wj}$ along the wheel rotation axis and, for the sake of simplicity, r is always the nominal wheel radius. These variables have been chosen because they are the most important physical quantities in a braking manoeuvre under degraded adhesion conditions. The variables coming from the 3D multibody model have been compared with the correspondent experimental quantities v_{wj}^{sp}, $r\omega_{wj}^{sp}$ (see Sect. 4).

Firstly, to better highlight the role played by the adhesion recovery in the 3D analysis of the complete vehicle dynamics, the authors report the comparison between the new degraded adhesion model and a classic adhesion model equal to the previous one but not taking into account the adhesion recovery due to the cleaning effect of the friction forces (Fig. 30).

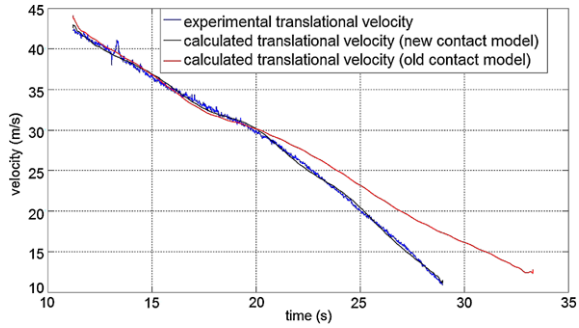

Fig. 30 Experimental velocity v_{w1}^{sp}, the velocity provided by the new model v_{w1}^{new} and the velocity provided by the classic model v_{w1}^{cl} for the I test of group A

The comparison (performed for the I test of group A) focuses on the translational velocities of vehicle wheels: the experimental velocity v_{w1}^{sp}, the velocity provided by the new model v_{w1}^{new} and the velocity v_{w1}^{cl} provided by the classic model. This simple example well underlines the importance of the adhesion recovery (caused by the energy dissipation at the contact interface) during the braking of railway vehicles under degraded adhesion conditions. More particularly such example effectively highlights the absence of adhesion recovery in the second phase of the braking manoeuvre, in disagreement with the experimental data.

Secondly, by way of example the time histories of the translational velocities v_{w1}, v_{w1}^{sp} and the rotational velocities $r\omega_{w1}$, $r\omega_{w1}^{sp}$ are reported in Figs. 31, 32, 33 and Figs. 34, 35, 36 for all the three tests of the groups A and B.

Additionally the maximum velocity errors E_j for all the performed tests are considered as well (see the Table 6 for E_1):

$$E_j = \max_{t\in[T_I,T_F]} \left| v_{wj}^{sp} - v_{wj} \right|. \tag{22}$$

The results of the analysis show a good agreement in terms of translational velocities v_{wj}, v_{wj}^{sp}, especially in the second part of the braking manoeuvre where the adhesion recovery occurs. Concerning the rotational velocities $r\omega_{wj}$, $r\omega_{wj}^{sp}$ (and thus the angular velocities) the matching is satisfying. However these physical quantities cannot be locally compared to each other because of the complexity and the chaoticity of the system due, for instance, to the presence of discontinuous and non-linear threshold elements like the WSP.

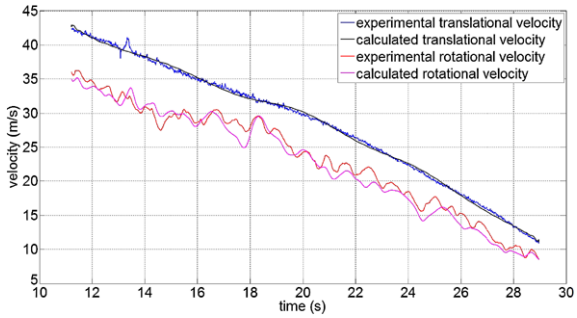

Fig. 31 Translational velocities v_{w1}, v_{w1}^{sp} and rotational velocities $r\omega_{w1}$, $r\omega_{w1}^{sp}$ of the I test of the group A

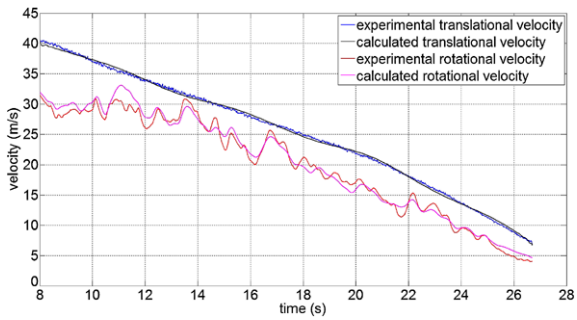

Fig. 32 Translational velocities v_{w1}, v_{w1}^{sp} and rotational velocities $r\omega_{w1}$, $r\omega_{w1}^{sp}$ of the II test of the group A

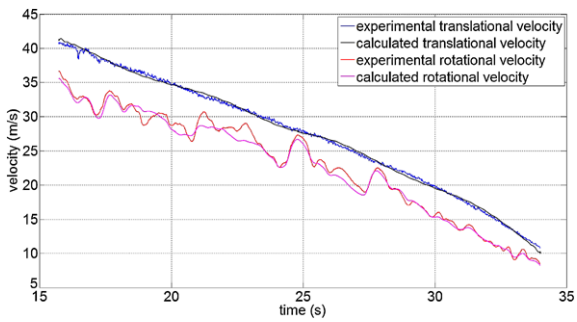

Fig. 33 Translational velocities v_{w1}, v_{w1}^{sp} and rotational velocities $r\omega_{w1}$, $r\omega_{w1}^{sp}$ of the III test of the group A

To better evaluate the behaviour of $r\omega_{wj}$ and $r\omega_{wj}^{sp}$ from a global point of view, it is useful to introduce the statistical means $\bar{s}_j$, $\bar{s}_j^{sp}$ and standard deviations Δ_j, Δ_j^{sp} of the calculated slidings s_j and of the experimental ones s_j^{sp}:

$$\begin{aligned} s_j &= v_{wj} - r\omega_{wj} \\ s_j^{sp} &= v_{wj}^{sp} - r\omega_{wj}^{sp}; \end{aligned} \tag{23}$$

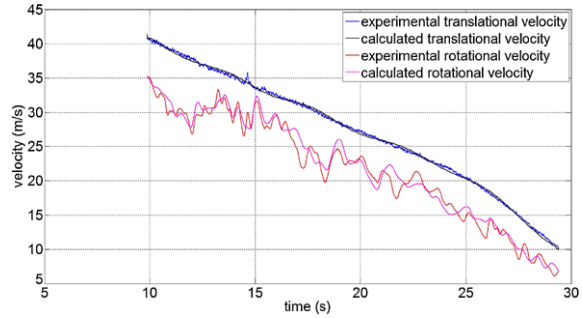

Fig. 34 Translational velocities v_{w1}, v_{w1}^{sp} and rotational velocities $r\omega_{w1}$, $r\omega_{w1}^{sp}$ of the I test of the group B

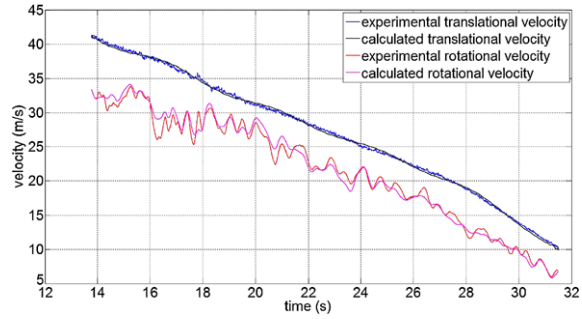

Fig. 35 Translational velocities v_{w1}, v_{w1}^{sp} and rotational velocities $r\omega_{w1}$, $r\omega_{w1}^{sp}$ of the II test of the group B

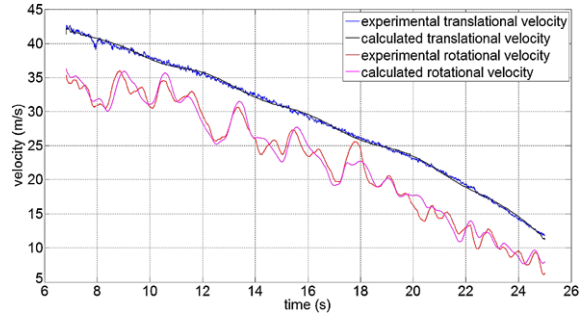

Fig. 36 Translational velocities v_{w1}, v_{w1}^{sp} and rotational velocities $r\omega_{w1}$, $r\omega_{w1}^{sp}$ of the III test of the group B

Table 6 Maximum velocity errors E_1, sliding means $\bar{s}_1$, $\bar{s}_1^{sp}$ and sliding standard deviations Δ_1, Δ_1^{sp}

Parameter	Units	A1	A2	A3	B1	B2	B3
E_1	[m/s]	2.05	0.90	1.84	1.51	0.91	1.68
$\bar{s}_1^{sp}$	[m/s]	5.00	5.25	4.23	5.49	5.41	5.83
$\bar{s}_1$	[m/s]	5.61	4.96	4.61	5.14	5.30	5.73
Δ_1^{sp}	[m/s]	1.72	2.19	1.59	1.75	1.77	1.78
Δ_1	[m/s]	1.49	1.79	1.59	1.58	1.45	1.84

the statistical indices are then evaluated as follows:

$$\begin{aligned}
\bar{s}_j &= \frac{1}{T_F - T_I}\int_{T_I}^{T_F} s_j dt \\
\bar{s}_j^{sp} &= \frac{1}{T_F - T_I}\int_{T_I}^{T_F} s_j^{sp} dt \\
\Delta_j &= \sqrt{\frac{1}{T_F - T_I}\int_{T_I}^{T_F} (s_j - \bar{s}_j)^2 dt} \\
\Delta_j^{sp} &= \sqrt{\frac{1}{T_F - T_I}\int_{T_I}^{T_F} \left(s_j^{sp} - \bar{s}_j^{sp}\right)^2 dt}
\end{aligned} \tag{24}$$

where T_I and T_F are initial and final times of the simulation respectively. For instance the means $\bar{s}_1$, $\bar{s}_1^{sp}$ and the standard deviations Δ_1, Δ_1^{sp} of the slidings s_1, s_j^{sp} are summarised in Table 6 for all the three tests of the groups A and B; they confirm the good matching also in terms of slidings and rotational velocities.

In conclusion, the numerical simulations of the vehicle dynamics during the braking manoeuvre highlight again the capability of the developed model in approximating the complex and highly non-linear behaviour of the degraded adhesion. The result is encouraging especially considering the simplicity of the whole model (only one unknown parameter is involved) and the computational times are very low.

7 Computational times

As previously said inside the paper, the wheel-rail contact model comprising the new degraded adhesion model is suitable for multibody applications, very important in the study of the railway vehicle dynamics. In particular high computational performances are required so that the contact model could be directly implemented online within more general multibody models developed in dedicated environments (in this case Matlab-Simulink) [1, 2].

The data corresponding to the CPU employed in the numerical simulations (see Sect. 6) and the main integration parameters of the ordinary differential equations (ODE) solver are reported in Table 7 [1, 44].

To verify the computational efficiency of the new degraded adhesion model, the simulation times concerning the whole railway vehicle model (3D multibody model of the vehicle and 3D wheel rail contact model) have been measured. The computation times reported in Table 8 are referred to the I test of the group A and are divided into the computation times related to the 3D multibody vehicle model and the ones related to the 3D wheel-rail contact model. More particularly, four different contact models (always implemented directly online within the multibody model of the vehicle) have been considered. All the contact models share the same contact point detection algorithm [10, 22, 34] and the solution of the normal problem [6, 11, 29] while, as regards the tangential contact problem, the following options have been taken into account: the global Kalker theory saturated through the Johnson-Vermeulen formula [28, 29], the Kalker FASTSIM algorithm [29, 30], the Polach model [38, 39] and the new degraded adhesion model.

As the results summarised in Table 8 show, the numerical efficiency of the new degraded adhesion model is substantially the same of the other wheel-rail contact models that do not consider degraded adhesion conditions. The achievement of this goal has been possible thanks to the simplicity of the new procedure and allows an easy and efficient online implementability of the adhesion model within more generic multibody models.

Table 7 CPU data and integration parameters

Parameter	Units	Parameter
CPU	–	INTEL Xeon E5430 2.66 GHz, 8 GB RAM
Integrator type	–	ODE5
Algorithm	–	Dormand-Prince
Order	–	5
Step type	–	Fixed
Stepsize Δt	[s]	10^{-4}

Table 8 Computation times of the different wheel-rail contact models

Contact model type	3D multibody vehicle model	3D contact model	Whole model
Global Kalker theory	232 s	118 s	350 s
Kalker FASTSIM algorithm	235 s	213 s	449 s
Polach model	232 s	128 s	360 s
New degraded adhesion model	232 s	130 s	362 s

8 Conclusions and further developments

In this paper the authors described a model aimed to obtain a better accuracy in reproducing degraded adhesion conditions in vehicle dynamics and railway systems. The followed approach turns out to be quite suitable for the multibody modelling (for instance in Matlab-Simulink and Simpack environments), a very important tool in the considered research areas; furthermore it assures high computational performances that permit to implement the degraded adhesion model direct online within more general multibody models of railway vehicles.

The innovative model focuses on the main phenomena characterising the degraded adhesion: the energy dissipation at the contact interface, the consequent cleaning effect and the resulting adhesion recovery due to the removal of external unknown contaminants. Moreover, the simplicity of the followed approach allows the minimisation of the number of hardly measurable physical quantities required by the model. This interesting feature is fundamental because most of the physical characteristics of the contaminants are totally unknown in practise.

The new adhesion model has been validated through experimental data provided by Trenitalia S. p. A. and coming from on-track tests carried out in Velim (Czech Republic) on a straight railway track characterised by degraded adhesion conditions. The tests have been performed with the railway vehicle UIC-Z1 equipped with a fully-working Wheel Slide Protection (WSP) system.

Concerning the future developments, firstly further and more exhaustive experimental campaigns are currently being carried out by Trenitalia and Rete Ferroviaria Italiana to test the new degraded adhesion model on a large number of different scenarios and, in particular, on generic curvilinear tracks (negotiating them at different travelling speeds and with different kinds and levels of contaminants). The new experimental data will allow a better tuning of the model geometrical and physical parameters and a better validation of the model itself. The model will be also compared to other contact models which do not consider the adhesion recovery to better investigate the role of this phenomenon.

Secondly many model improvements will be taken into account. More particularly, new theoretical and experimental relations among the adhesion coefficient f, the specific dissipated energy W_{sp} and the limit adhesion levels f_d, f_r (degraded adhesion and adhesion recovery) will be introduced and analysed. This way the physical origin and meaning of the transition function $\lambda(W_{sp})$ will be better investigated, trying to connect it to more elementary physical and tribological phenomena (for example phenomena related to wear of the wheel and rail profiles on which the authors have recently worked; see for instance the references [9, 25, 53, 54]).

Finally the new degraded adhesion model will be implemented within 3D multibody models of different railway vehicles (developed in dedicated environments like Matlab-Simulink, Simpack, etc.) operating on generic railway tracks. This way the degraded adhesion effect on the railway vehicle dynamics, the wheel-rail contact and the wear affecting the wheel and rail surfaces will be better investigated.

Acknowledgements The authors would like to thank the Trenitalia archives for supplying the experimental data relative to the braking tests under degraded adhesion conditions.

References

1. Official Site of Mathworks, Natick, MA, USA (2012). www.mathworks.com
2. Official Site of Simpack GmbH, Gilching, Germany (2012). www.simpack.com
3. UNI EN 15595 (2009) Railway applications, braking, wheel slide protection. Milano, Maggio
4. Allotta B, Conti R, Malvezzi M, Meli E, Pugi L, Ridolfi A (2012) Numerical simulation of a HIL full scale roller-rig model to reproduce degraded adhesion conditions in railway applications. In: European Congress on computational methods in applied sciences and engineering (ECCOMAS 2012), Austria
5. Allotta B, Malvezzi M, Pugi L, Ridolfi A, Rindi A, Vettori G (2012) Evaluation of odometry algorithm performances using a railway vehicle dynamic model. Veh Syst Dyn 50(5):699–724
6. Antoine J, Visa C, Sauvey C, Abba G (2006) Approximate analytical model for hertzian elliptical contact problems. J Tribol 128:660–664
7. Arias-Cuevas O, Li Z, Lewis R (2011) A laboratory investigation on the influence of the particle size and slip during sanding on the adhesion and wear in the wheel–rail contact. Wear 271:14–24
8. Arias-Cuevas O, Li Z, Lewis R, Gallardo-Hernandez E (2010) Rolling–sliding laboratory tests of friction modifiers in dry and wet wheel–rail contacts. Wear 268:543–551
9. Auciello J, Ignesti M, Marini L, Meli E, Rindi A (2013) Development of a model for the analysis of wheel wear in railway vehicles. Meccanica 48(3):681–697

10. Auciello J, Meli E, Falomi S, Malvezzi M (2009) Dynamic simulation of railway vehicles: wheel/rail contact analysis. Veh Syst Dyn 47:867–899
11. Ayasse J, Chollet H (2005) Determination of the wheel rail contact patch in semi-hertzian conditions. Veh Syst Dyn 43:161–172
12. Blau PJ (2009) Embedding wear models into friction models. Tribol Lett 34:75–79
13. Boiteux M (1986) Le probleme de l'adherence en freinage. Revue generale des chemins de fer pp 59–72
14. Carbone G, Bottiglione F (2011) Contact mechanics of rough surfaces: a comparison between theories. Meccanica 46(3):557–665
15. Cheli F, Pennestri E (2006) Cinematica e dinamica dei sistemi multibody. CEA, Milano
16. Chen H, Ban T, Ishida M, Nakahara T (2008) Experimental investigation of influential factors on adhesion between wheel and rail under wet conditions. Wear 265:1504–1511
17. Conti B, Meli E, Pugi L, Malvezzi M, Bartolini F, Allotta B, Rindi A, Toni P (2012) A numerical model of a hil scaled roller rig for simulation of wheel–rail degraded adhesion condition. Veh Syst Dyn 50(5):775–804
18. Descartes S, Desrayaud C, Niccolini E, Berthier Y (2005) Presence and role of the third body in a wheel–rail contact. Wear 258:1081–1090
19. Dukkipati R, Amyot J (1988) Computer aided simulation in railway dynamics. Dekker, New York
20. Eadie D, Kalousek J, Chiddick K (2002) The role of high positive friction (hpf) modifier in the control of short pitch corrugations and related phenomena. Wear 253:185–192
21. Esveld C (2001) Modern railway track. Delft University of Technology, Delft
22. Falomi S, Malvezzi M, Meli E (2011) Multibody modeling of railway vehicles: innovative algorithms for the detection of wheel–rail contact points. Wear 271(1–2):453–461
23. Falomi S, Malvezzi M, Meli E, Rindi A (2009) Determination of wheel–rail contact points: comparison between classical and neural network based procedures. Meccanica 44(6):661–686
24. Gallardo-Hernandez E, Lewis R (2008) Twin disc assessment of wheel/rail adhesion. Wear 265:1309–1316
25. Ignesti M, Malvezzi M, Marini L, Meli E, Rindi A (2012) Development of a wear model for the prediction of wheel and rail profile evolution in railway systems. Wear 284–285:1–17
26. Iwnicki S (2003) Simulation of wheel–rail contact forces. Fatigue Fract Eng Mater Struct 26:887–900
27. Iwnicki S (2006) Handbook of railway vehicle dynamics. Taylor & Francis, London
28. Johnson K (1985) Contact mechanics. Cambridge University Press, Cambridge
29. Kalker J (1990) Three-dimensional elastic bodies in rolling contact. Kluwer Academic, Norwell
30. Kalker JJ (1982) A fast algorithm for the simplified theory of rolling contact. Veh Syst Dyn 11:1–13
31. Kelley C (1995) Iterative methods for linear and nonlinear equations. SIAM, Philadelphia
32. Magheri S, Malvezzi M, Meli E, Rindi A (2011) An innovative wheel–rail contact model for multibody applications. Wear 271(1–2):462–471
33. Malvezzi M, Pugi L, Ridolfi A, Cangioli F, Rindi A (2011) Three dimensional modelling of wheel–rail degraded adhesion conditions. In: Proceedings of IAVSD 2011, Manchester
34. Meli E, Falomi S, Malvezzi M, Rindi A (2008) Determination of wheel–rail contact points with semianalytic methods. Multibody Syst Dyn 20(4):327–358
35. Meli E, Pugi L, Ridolfi A (2013) An innovative degraded adhesion model for multibody applications in the railway field. Multibody Syst Dyn. doi:10.1007/s11044-013-9400-9
36. Niccolini E, Berthier Y (2005) Wheel–rail adhesion: laboratory study of "natural" third body role on locomotives wheels and rails. Wear 258:1172–1178
37. Nocedal J, Wright S (1999) Numerical optimisation. Springer series in operation research. Springer, Berlin
38. Polach O (1999) A fast wheel–rail forces calculation computer code. Veh Syst Dyn 33:728–739
39. Polach O (2005) Creep forces in simulations of traction vehicles running on adhesion limit. Wear 258:992–1000
40. Pombo J, Ambrosio J (2008) Application of a wheel–rail contact model to railway dynamics in small radius curved tracks. Multibody Syst Dyn 19:91–114
41. Pombo J, Silva A (2007) A new wheel–rail contact model for railway dynamics. Veh Syst Dyn 45:165–189
42. Shabana A, Tobaa M, Sugiyama H, Zaazaa K (2005) On the computer formulations of the wheel/rail contact problem. Nonlinear Dyn 40:169–193
43. Shabana A, Zaazaa K, Escalona JE, Sany JR (2004) Development of elastic force model for wheel/rail contact problems. J Sound Vib 269:295–325
44. Shampine L, Reichelt M (1997) The Matlab ode suite. SIAM J Sci Comput 18:1–22
45. Tasora A, Anitescu M (2013) A complementarity-based rolling friction model for rigid contacts. Meccanica 48(7):1643–1659
46. TrenitaliaSpA: UIC-Z1 coach (2000) Internal report of Trenitalia, Rome, Italy
47. TrenitaliaSpA: On-track braking tests (2005) Internal report of Trenitalia, Rome, Italy
48. TrenitaliaSpA: WSP systems (2006) Internal report of Trenitalia, Rome, Italy
49. Voltr P, Lata M, Cerny O (2012) Measuring of wheel–rail adhesion characteristics at a test stand. In: XVIII international conference on engineering mechanics, Czech Republic
50. Wang W, Zhang H, Wang H, Liu Q, Zhu M (2011) Study on the adhesion behaviour of wheel/rail under oil, water and sanding conditions. Wear 271:2693–2698
51. Zhang W, Chen J, Wu X, Jin X (2002) Wheel/rail adhesion and analysis by using full scale roller rig. Wear 253:82–88
52. Allotta B, Meli E, Ridolfi A, Rindi A (2013) Development of an innovative wheel-rail contact model for the analysis of degraded adhesion in railway systems. Tribol Int 69:128–140
53. Auciello J, Ignesti M, Malvezzi M, Meli E, Rindi A (2012) Development and validation of a wear model for the analysis of the wheel profile evolution in railway vehicles. Veh Syst Dyn 50(11):1707–1734
54. Innocenti A, Marini L, Meli E, Pallini G, Rindi A (2013) Development of a wear model for the analysis of complex railway networks. Wear. doi:10.1016/j.wear.2013.11.010